

## Design and optimization of near-field thermophotovoltaic systems using deep learning

A.A. Odebowale<sup>✉,\*</sup>, Khalil As'ham, Haroldo T. Hattori, and Andrey. E. Miroshnichenko<sup>†</sup>  
*School of Engineering and Technology, The University of New South Wales Canberra, Northcott Drive,  
 Campbell, Canberra, Australian Capital Territory 2600, Australia*



(Received 29 June 2023; revised 18 May 2024; accepted 22 May 2024; published 13 June 2024)

Extensive research has been conducted on near-field radiative heat transfer (NFRHT) due to its wide range of applications in energy conversion, radiative cooling, and thermal diodes. The main objective of studying NFRHT at the nanoscale gap is to enhance system performance. This research proposes a new approach to designing and optimizing a near-field thermophotovoltaic (NFTPV) system using deep-learning techniques. Our study utilizes a fully connected network (FCN) and an automated-machine-learning (AutoML) model to simulate radiative heat transfer, aiming to improve radiative heat flux, power generation, and overall system efficiency. By comparing two emitter configurations, we find that the hyperbolic emitter outperforms other configurations, as evidenced by its impact on various system-performance parameters. Significant achievements have been made through our investigations. For the SiC-plate emitter configuration, we have achieved a notable power density of  $0.589 \text{ W/cm}^2$  and an efficiency of 23% after accounting for nonradiative recombination at a temperature difference of 600 K with a 100-nm gap. Moreover, the four-period emitter configuration has yielded even more impressive results, with a power density of  $0.9452 \text{ W/cm}^2$  and an efficiency of 30% after accounting for nonradiative recombination. This study demonstrates the immense potential of utilizing FCN and AutoML for theoretical modeling and optimization of structural parameters in NFTPV systems, as well as providing an accurate model for predicting photocurrent generation. By highlighting the capabilities of these advanced techniques, we have hopefully paved the way for further advancements and innovations in NFRHT.

DOI: [10.1103/PhysRevApplied.21.064031](https://doi.org/10.1103/PhysRevApplied.21.064031)

### I. INTRODUCTION

Near-field thermal radiation has recently garnered significant attention due to its compelling applications in a variety of fields, including but not limited to nanoscale-gap thermophotovoltaic (TPV) power generation [1–5], thermal lithography [6], thermal imaging [7], scanning thermal microscopy [8,9], heat-assisted magnetic recording [10,11], advanced thermal management [12–15], and thermal logic devices. Additionally, it has been explored for its potential in other energy-conversion devices [16,17]. Near-field thermophotovoltaic (NFTPV) systems present a promising avenue for direct conversion of heat into electricity, offering remarkably high power output and efficiencies comparable to, or even surpassing, those reported for far-field TPV systems. The potential for power enhancements beyond the black-body limit positions TPV systems as strong contenders against thermoelectric systems. Conventional TPV systems have low power output and conversion-efficiency limitations, which limit their practical applications. However, near-field thermal radiation,

which enhances radiative heat transfer beyond Planck's law in the far-field regime, has been introduced into the TPV system to address these limitations. This approach has been demonstrated by various studies to improve the performance of the system and overcome these limitations [18–20]. This technology offers several advantages, including its ecofriendliness, lack of moving parts, and ability to adapt to various heat sources. Experimental studies on the near-field effect in thermal radiation have also propelled the field forward by demonstrating the ability to surpass the Stefan-Boltzmann law in the far field [1–5,21–24]. This phenomenon arises from the contribution of evanescent fields (photon tunnelling) when objects exchanging thermal radiation are in close proximity: the gap between them is less than the thermal wavelength ( $\lambda_{th}$ ), which is approximately  $10 \text{ }\mu\text{m}$  at room temperature. Mittapally *et al.* have recently conducted a comprehensive review focusing on the fundamental principles of radiative heat transfer across various application domains. They have also highlighted potential future prospects for advancing NFTPV systems. The review has encompassed an analysis of recent experimental platforms that effectively addresses multiple challenges encountered in exploring NFTPV system. Their review delves into related

\*Corresponding author: [a.odebowale@adfa.edu.au](mailto:a.odebowale@adfa.edu.au)

<sup>†</sup>Corresponding author: [andrey.miroshnichenko@unsw.edu.au](mailto:andrey.miroshnichenko@unsw.edu.au)

photonic energy-conversion techniques, including thermoradiative and thermophotonic power generation. They have concluded their discussion with an exploration of future opportunities for scaling up NFTPV systems and enhancing their overall performance [25]. As highlighted in Ref. [25], achieving high power output and efficiency involves implementing diverse strategies. These include engineering emitters to emit selectively in the above-band-gap region while minimizing absorption in the sub-band-gap region, adjusting dielectric properties [26], and the choice of materials, particularly those that support surface modes at the interface between the object and the vacuum. Examples include polar dielectrics such as silicon dioxide ( $\text{SiO}_2$ ) and silicon nitride ( $\text{SiN}$ ), as well as metals having surface plasmon polaritons in the infrared region of the electromagnetic spectrum. Other approaches involve developing thin-film and multilayer structures that exhibit multiple surface modes [27–29], employing metasurfaces [30,31] and utilizing nonreciprocal materials [32]. Consequently, researchers have been exploring different combinations of metals and dielectrics in their designs, resulting in hyperbolic metamaterials (HMMs) that have contributed significantly to the enhancement of the radiative heat flux [24,33,34]. Datas and Vailan have conducted a theoretical analysis of a device that involves the transmission of photons and electrons from a hot  $\text{LaB}_6$ -coated tungsten emitter to a closely spaced  $\text{BaF}_2$ -coated  $\text{InGaAs}$  photovoltaic cell. This device utilizes photon tunneling and space-charge removal across a nanoscale vacuum gap to significantly enhance the flux of electrons and photons, thereby boosting the generated electrical power density. Their research has resulted in impressive conversion efficiencies and electrical power densities of approximately 30% and  $70 \text{ W/cm}^2$ , respectively, at 2000 K, with a practical gap distance of 100 nm. These achievements mark a substantial improvement over the performance of stand-alone near-field thermophotovoltaic devices, which typically exhibit efficiencies of around 10% and power densities of approximately  $10 \text{ W/cm}^2$  [35]. In a separate study, Jin *et al.* have explored the performance of a near-field thermophotovoltaic (NFTPV) energy-conversion system. In their setup, a  $\text{W/SiO}_2$ -multilayer-based hyperbolic metamaterial (HMM) served as the emitter at 1000 K, while  $\text{InAs}$  acted as the TPV cell at 300 K. Their findings demonstrate that the use of HMM results in a sixfold increase in the electric power of the NFTPV devices compared to those employing a plain W emitter, this being particularly evident at a 100-nm vacuum gap [34]. Lim *et al.* have achieved significant performance enhancement in an NFTPV system by introducing a hyperbolic metamaterial (HMM) emitter, multilayered graphene, and an Au-backside reflector. The HMM emitter and multilayered graphene-covered TPV cell have been optimized using a genetic algorithm to maximize the system power output. Compared to a system with a bulk emitter and a bare

TPV cell, the optimized configuration has resulted in a remarkable 24.2-fold increase in power output [36].

Advancements in deep-learning architectures, algorithms, computational tools, and access to large data sets have had a tremendous impact across various fields such as science, engineering, and medicine [37–39]. In photonics, deep learning has been utilized for modeling, designing, and optimizing photonics devices more efficiently and quickly than traditional numerical modeling methods. The application of deep learning in the field of radiative heat transfer at a nanoscale gap has recently become a topic of interest. In the past few years, the progress of machine-learning (ML) algorithms and the availability of open-source software have opened up new avenues for researchers to address optimization challenges in near-field radiative heat transfer. The appealing benefits of ML, such as the ability to identify multidimensional correlations and explore vast design spaces, have piqued the interest of thermal-science researchers, who have successfully integrated ML into their work, bringing novel perspectives to traditional problems. As a result, a significant number of researchers in the field of thermal radiation are now creating ML-assisted code that can effectively optimize structures for specific objectives [40–43]. The area of ML application in thermal-radiation research has primarily concentrated on the application of radiative heat transfer in the far-field regime. However, there is a growing interest in exploring the potential of ML in effectively addressing optimization challenges in near-field radiative heat transfer (NFRHT). Despite this interest, much is still to be discussed about how ML can be successfully applied in this field. To address this gap, Wen *et al.* have developed an ML strategy that utilizes data-driven approaches, specifically an artificial neural network (ANN) and a genetic algorithm (GA) combination. The authors have proposed a systematic work flow for the modeling and optimal design of NFRHT using this strategy. Their work provides valuable insights into the potential of ML to optimize NFRHT and contributes to the growing body of research in this area [44]. García-Esteban *et al.* have showcased the effective application of artificial neural networks (ANNs) in theoretical modeling and analysis across a diverse range of radiative-heat-transfer phenomena and devices. Their study has encompassed three distinct application domains, namely, NFRHT involving multilayer systems forming hyperbolic metamaterials (HMMs), passive radiative cooling in photonic crystal slab structures, and thermal emission from subwavelength objects [41]. Their work is the driving force behind this present comparative study. This study compares theoretical modeling techniques for the radiative heat flux in an NFTPV system. No comparative study has been conducted to evaluate the effectiveness of fully connected networks (FCNs) and automated machine learning (AutoML) in designing and optimizing NFRHT for energy conversion in NFTPV systems. This study

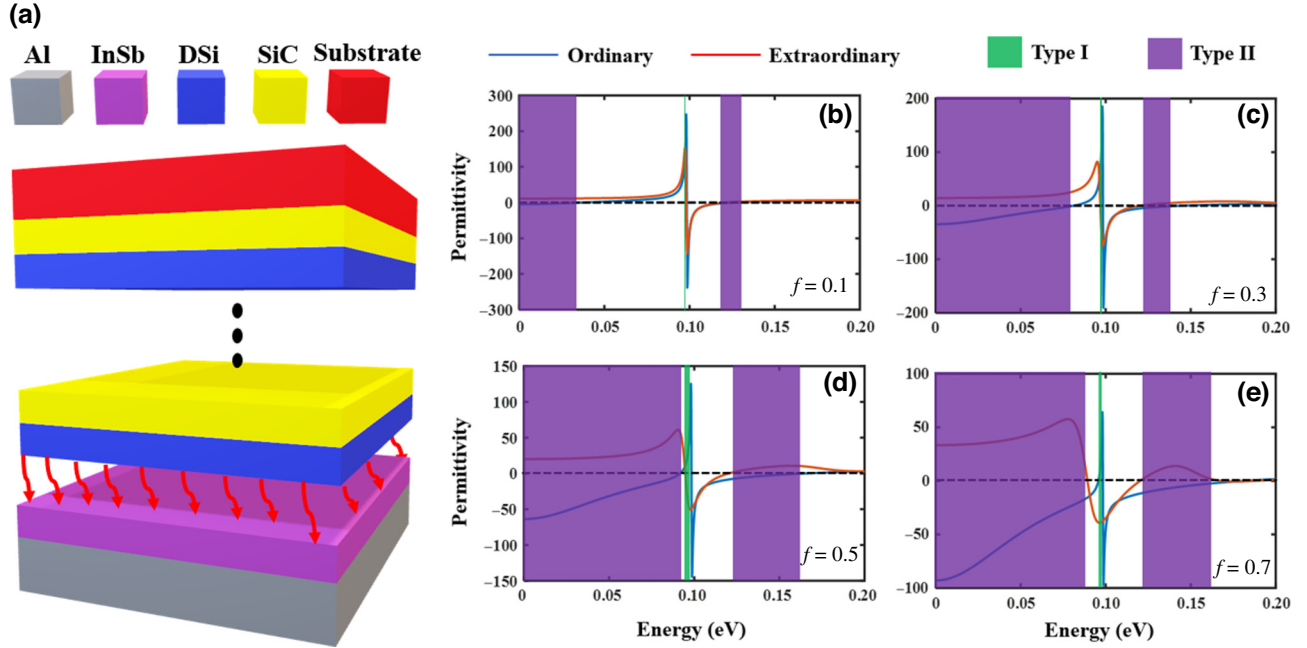


FIG. 1. (a) A schematic of an NFTPV system. (b)–(e) Plots of permittivities for a DSi/SiC hyperbolic structure at different filling fractions at a doping concentration of  $10^{19} \text{ cm}^{-3}$ . Type I (green) and Type II (violet) hyperbolic bands spread across the SiC reststrahlen band. Type I occurs in the second quadrant, where the real parts of the ordinary ( $\epsilon_{\perp} > 0$ ) (blue line) and extraordinary ( $\epsilon_{\parallel} < 0$ ) (red line) dielectric functions are positive and negative, respectively, while Type II occurs in the fourth quadrant, where the real parts of the ordinary dielectric functions are negative ( $\epsilon_{\perp} < 0$ ) and those of the extraordinary ( $\epsilon_{\parallel} > 0$ ) dielectric functions are positive.

addresses this gap by conducting a comparative analysis of these two approaches. The results of this study may provide valuable insights into the potential of FCN and AutoML in optimizing NFRHT for energy conversion. We aim to enhance the performance of the NFTPV system by generating a high radiative heat flux, which is a crucial factor for an efficient NFTPV system. The emitter comprises periodic layers of doped silicon (DSi) and silicon carbide (SiC) media arranged on a semi-infinite substrate, forming a hyperbolic metamaterial (HMM) structure. DSi and SiC are used as metallic and dielectric layers, respectively. Meanwhile, the receiver is composed of an indium antimonide (InSb) layer on a semi-infinite aluminum (Al) layer, which serves as a metallic contact, as depicted in Fig. 1(a). We conduct theoretical modeling of NFRHT using a fluctuation electrodynamics (FE) framework that employs dyadic Green's functions (DGFs) and the scattering matrix (SM).

## II. RESULTS AND DISCUSSION

An understanding of the structural characteristics of emitters is crucial for optimizing their performance in various applications. We delve into the utilization of effective medium theory (EMT) to model the dielectric function of emitter structures, focusing in particular on establishing their hyperbolic nature. The emitter structure under study comprises alternating layers of DSi and SiC materials,

arranged on top of a semi-infinite substrate. The selection of materials for constructing the emitter depends on their capability to support surface waves, which is a crucial factor in emitter design considerations. SiC can be manufactured by combining silica sand and carbon in an Acheson graphite electric resistance furnace at temperatures ranging from  $1600^{\circ}\text{C}$  ( $2910^{\circ}\text{F}$ ) to  $2500^{\circ}\text{C}$  ( $4530^{\circ}\text{F}$ ) [45]. Alternatively, SiC nanopowder can be synthesized using silica fume [46]. Silicon (Si) is typically manufactured using standard semiconductor processes and can be doped to form DSi. By employing well-established EMT expressions, we determine the dielectric function of this structure, facilitating the identification of Type-I and Type-II hyperbolic media based on the dielectric properties of the constituent materials. Type I occurs in a region where the real parts of the ordinary ( $\epsilon_{\perp} > 0$ ) and extraordinary ( $\epsilon_{\parallel} < 0$ ) permittivity are positive and negative, respectively, while Type II occurs in a region where the real parts of the ordinary ( $\epsilon_{\perp} < 0$ ) and extraordinary ( $\epsilon_{\parallel} > 0$ ) permittivity are negative and positive, respectively. The permittivity values for DSi are sourced from Ref. [47], while those for SiC and other materials pertinent to the thermophotovoltaic (TPV) cell, such as aluminum (Al) and indium antimonide (InSb), are detailed in Sec. IV. To establish the existence of the hyperbolic media, we present the plots of the real parts of the effective permittivities of DSi/SiC nanostructures at different filling ratios ( $f = 0.1$ – $0.7$ ) as shown in Figs. 1(b)–1(e). We observe that the width of

the hyperbolic bands can be controlled by varying the filling ratio  $f$ , with the largest width achieved at  $f = 50\%$ . These plots not only confirm the presence of Type-I and -II hyperbolic structures but also show their extension toward the SiC reststrahlen bands: a region in which SiC exhibits metallic behavior [48]. While the use of EMT has been associated with inaccurate predictions of radiative heat transfer, the EMT expression remains a useful tool for determining the frequency bands of HMM. It is important, however, to exercise caution when applying the expression. One approach to broadening the hyperbolic bands is to use two adjacent reststrahlen bands from phonon-polaritonic materials such as SiC and GaN, as suggested by Biehs and Ben-Abdallah [48]. Although metals also exhibit negative permittivity over the bands, they tend to have a high loss in the infrared region, making them less advantageous than phonon-polaritonic materials, as noted by Land *et al.* [49].

Once we have established that the proposed emitter structure exhibits a hyperbolic structure through the emergence of Type I and II structures, as described previously, the next step is to determine the photonic transmission coefficient ( $\xi$ ) using Eq. (6). This analysis aims to provide a deeper understanding of how hyperbolic bands form and to examine the influence of the periodic layer of DSi/SiC on their development. We maintain the thickness of both

SiC and DSi layers at 10 nm for this investigation. This thickness corresponds to a filling ratio of 50%, which has been observed to produce the broadest hyperbolic bands, as depicted in Fig. 1(d). To calculate the reflection coefficients for the TE and TM modes, we adopt the approach presented in Ref. [50], as detailed in Sec. A, which we then apply to Eq. (6) to obtain  $\xi$ . This approach is used because of the problem associated with EMT when used in the prediction of radiative heat transfer. In Fig. 2, we illustrate a comparison of surface plots for various structural designs: single parallel surfaces and hyperbolic structures at different periods. In Fig. 2(a), surface modes exist between two SiC plates coupled via the material vacuum interface. In Figs. 2(b)–2(d), it can be observed that both surface modes and hyperbolic modes exist between HMMs. The amplitude of the hyperbolic mode increases while the spread decreases as the number of DSi/SiC layers increases due to the multiple reflections that occur at the interface between the media. The hyperbolic modes differ from surface modes as they propagate through the multi-layer media, in contrast to the localized nature of surface modes.

Next, we demonstrate radiative heat transfer between different emitter-design configurations and the TPV cell at an emitter temperature  $T_e$  and a receiver temperature  $T_r$  of 900 K and 300 K, respectively, when the vacuum

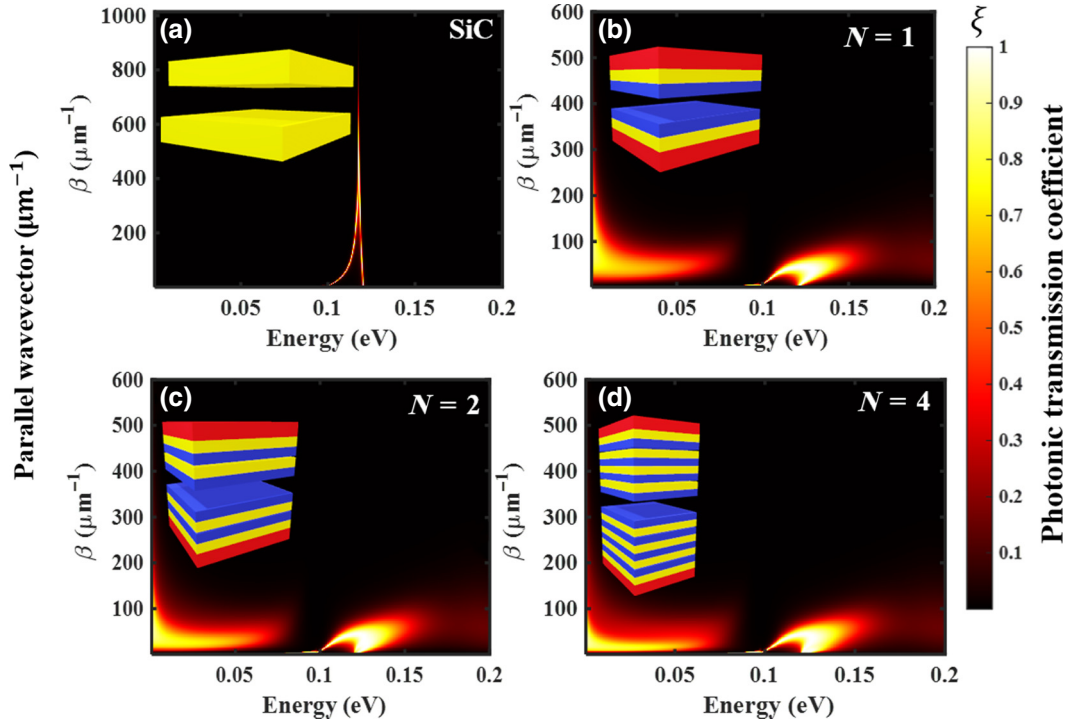


FIG. 2. The photonic transmission coefficient  $\xi$  for TM modes at  $d = 10$  nm. (a) Two bulk SiC plates. (b) A hyperbolic metamaterial (HMM) with a single period ( $N = 1$ ) shows the appearance of hyperbolic and surface modes. (c) A two-period HMM ( $N = 2$ ); here, the hyperbolic modes become more visible, together with the surface mode. (d) A four-period HMM ( $N = 4$ ); here, the hyperbolic modes become more visible together with the surface mode [as compared to (b) and (c)].



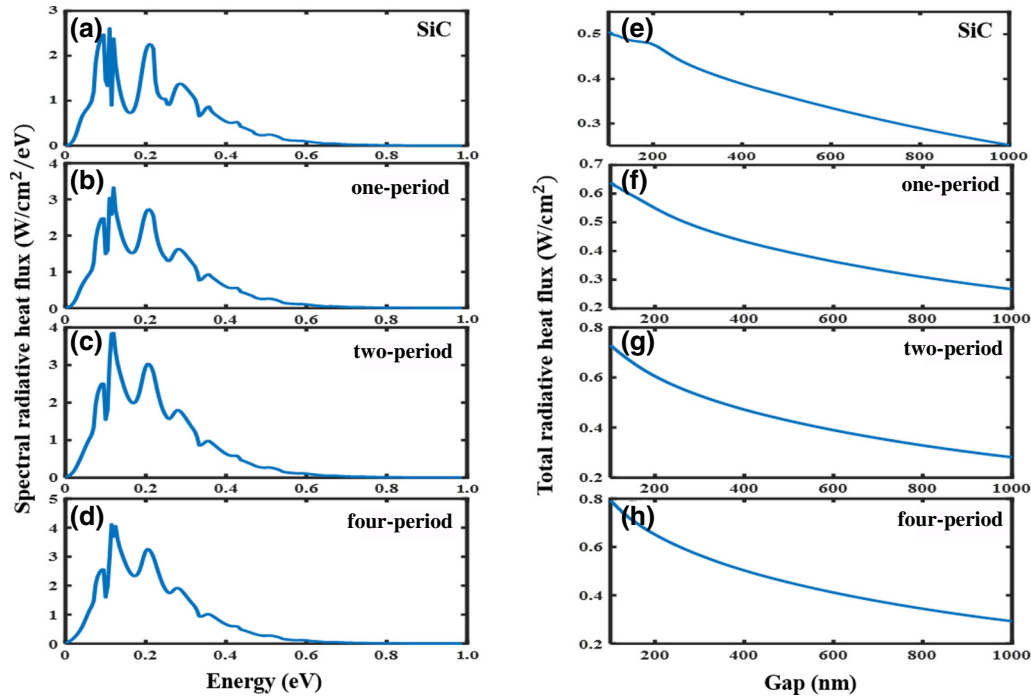


FIG. 3. (a)–(d) The spectral radiative heat flux and total heat flux for different emitter designs at a 100-nm vacuum gap: (a) the SiC-plate emitter; (b) the one-period emitter; (c) the two-period emitter; (d) the four-period emitter. (e) The total heat flux for the SiC-plate. (f) The total heat flux for the one-period emitter. (g) The total heat flux for the two-period emitter. (h) The total heat flux for the four-period emitter.

gap  $d$  is set at 100 nm. The different emitter designs under consideration include the SiC-plate and one-period HMM, two-period HMM, and four-period HMM emitters. The results are shown in Figs. 3(a)–3(d) and clearly demonstrate that the HMM emitters exhibit a higher peak in  $q_\omega$  at around 0.1 eV, which results in higher  $Q$  values, as shown in Figs. 3(e)–3(h), compared to the SiC-plate emitter. There is slight increase in the peak as the period increases, attributed to the contributions of both surface and hyperbolic modes becoming more pronounced as the number of periods increases. The maximum peak of  $q_\omega$  is observed for the four-period HMM emitter, outperforming other emitter designs. This emphasizes that utilizing hyperbolic structures as emitters significantly enhances  $q_\omega$  compared to modeling the emitter as a semi-infinite plate of SiC. To demonstrate the ability of the model to distinguish between structures with varying input parameters, we have performed an analysis on the response of the model to a varying structural layer and the results of this analysis can be found in Fig. 7.

Additionally, we have investigated how changes in the vacuum gap  $d$  between the emitter and receiver affect the total heat flux  $Q$  by examining various emitter designs. In Figs. 3(e)–3(h), we show the corresponding  $Q$  at different gaps for all emitter configurations. As expected,  $Q$  decreases as  $d$  increases. Across all emitter designs, the maximum net heat flux is achieved by the four-period

HMM emitter, followed by the two-period HMM and the one-period HMM, and the least by the SiC-plate, when  $d = 100$  nm. At a 100-nm gap, the recorded values of  $Q$  are 0.6390  $W/cm^2$ , 0.7292  $W/cm^2$ , 0.792582  $W/cm^2$ , and 0.505194  $W/cm^2$  for the one-period, two-period, and four-period HMM emitters and the SiC-plate emitter, respectively. At the specified gap, all HMM emitters have higher value of  $Q$  compared with the SiC-plate emitter. Notably, for a four-period emitter layer,  $Q$  is 1.6, 1.2, and 1.1 times higher than that of a SiC-plate (0.505194  $W/cm^2$ ), a one-period emitter (0.6390  $W/cm^2$ ), and a two-period emitter (0.7292  $W/cm^2$ ), respectively. Hence, the enhancement rate increases as the emitter period is increased from 1 to 4. We have also explored the impact of the doping concentration  $N_c$  of DSi on the  $Q$  enhancement for all HMM emitters at different gaps. The results demonstrate that by increasing  $N_c$  to  $10^{21}$  when  $d = 100$  nm, the values of  $Q$  obtained are 0.825375  $W/cm^2$ , 0.89  $W/cm^2$ , and 0.9031  $W/cm^2$  for one-period, two-period, and four-period HMM emitters, respectively. The increase in  $N_c$  results in an enhancement factor of 1.29, 1.22, and 1.14 times the values of  $Q$  obtained when  $N_c = 10^{20}$  for one-period, two-period, and four-period HMM emitters, respectively. Further details on the effect of  $N_c$  on  $Q$  can be found in Fig. 6. These findings underscore that HMM emitters yield higher values of  $Q$  compared to the single-plate emitter configuration. The results indicate that the same  $Q$  can be achieved at a larger

gap distance when using an HMM emitter than a single-plate emitter. This finding is significant for experimental research, as achieving a small gap distance is a challenging task that often requires an advanced experimental setup [51]. We have also demonstrated how changes in the emitter temperature  $T_e$  affect both the optical and electrical performance of our designs (see the details in Sec. B). First, we demonstrate how the temperature changes affect the  $Q$  values by systematically adjusting the emitter temperature across a range from 500 K to 1200 K. Our findings indicate that the effect of temperature elevation on the total heat flux is more prominently noticeable in the case of the HMM emitters when compared to the SiC-plate emitter. This distinction is visually depicted in Fig. 6(b).

To demonstrate how ML methods can be used in the theoretical design and optimization of the radiative heat flux for an NFTPV system for energy conversion, we employ an FCN and AutoML in our design. In Fig. 4(a), we illustrate a schematic representation of a forward modeling network used in our analysis. This network takes in the structure represented by  $t_1, \dots, t_n$  as input and generates a response denoted by  $\beta_1, \dots, \beta_n$  as output. Hidden layers with their respective neurons connect the input and output. We use a five-layer FCN with nine, 400, 400, 200, and 200 units, respectively, for our analysis. The input layer

of nine units represents the thickness of a nine-layer [an eight-layer HMM emitter and a one-layer InSb cell, shown in Fig. 4(b)], while the output of 200 units matches the number of discrete points of the radiative-heat-flux spectrum. The FCN has three hidden layers with 400, 400, and 200 units, respectively. We set the activation function to ReLU and use Adam as the optimizer, with a learning rate of  $1 \times 10^{-6}$  and 1000 epochs. We generate 1000 training data sets using the MATLAB software by varying  $t_1, \dots, t_9$  and obtaining the corresponding response, which is the spectral radiative flux ( $q_w$ ), in this case at a 100-nm vacuum gap for practicality [34]. The first eight structures ( $t_1, \dots, t_8$ ) vary from 10 to 50 nm, while  $t_9$  varies from 1 to 5  $\mu\text{m}$ . Training is conducted to minimize the cost function, which measures the average-squared difference between the predicted flux and the actual flux of the neural networks (NNs). In this process, 70% of the available data is utilized for training, while the rest is divided into validation and test sets. The learning curve, illustrated in Fig. 4(c), demonstrates that the FCN is appropriately trained, as evidenced by the gradual decrease in the loss function across the test samples.

As part of our comparative study, we have utilized AutoML to model the spectral radiative heat flux theoretically. AutoML is an advanced technique that automatically

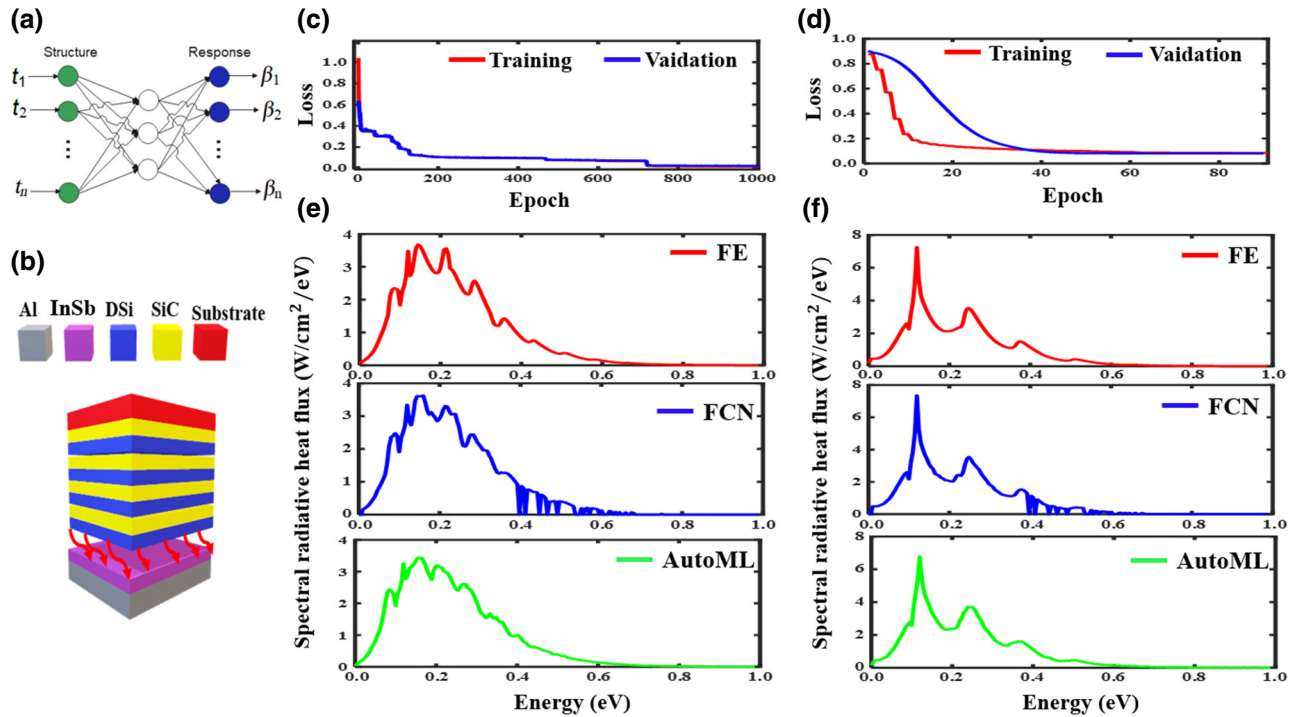


FIG. 4. (a) A fully connected network (FCN) model. (b) The schematic diagram of the NFTPV system at a 100-nm gap. (c) Training and validation against the epoch for FCN. (d) Training and validation against the epoch for AutoML. (e) A comparison of the spectral radiative-heat-flux predictions using ML models (FCN and AutoML) with the theoretical approach (FE) before optimization. (f) A comparison of the spectral radiative-heat-flux predictions using ML models (FCN and AutoML) with the theoretical approach (FE) after optimization.

discovers the best-performing model for a given data set. Unlike FCN, which requires the user to select the model architecture and hyperparameters, AutoML uses neural-architecture search (NAS) to determine both the model architecture and the hyperparameters used for training. This approach enables researchers to address predictive modeling tasks with minimal input efficiently. In our analysis, we have searched 15 models using NAS and found that the best-performing model generated by AutoML consists of a four-layer architecture with nine, 16, 32, and 200 units, respectively, a ReLU activation function, and an Adam optimizer. We have plotted the loss function against epoch for both training and test instances in Fig. 4(d) and compared the  $q_\omega$  values predicted by both the FCN and AutoML models to those obtained from FE in Fig. 4(e) when the structure was set to 10 nm, 50 nm, 20 nm, 40 nm, 15 nm, 10 nm, 20 nm, 30 nm, and 2000 nm.

We have followed an iterative algorithm to optimize the structural parameter of the NFTPV system (the layer thickness), using both the FCN and AutoML models. This algorithm is represented by a schematic diagram in Fig. 9. In this algorithm, we compare the predictions of the  $\beta_i$  to  $\beta_{i+1}$ , where  $i$  varies from 1 to the length of the design space. This process continues until it covers the entire design space and finally produces the peak spectrum  $\beta_{\max}$  and the corresponding structure. Our goal has been to generate the highest possible  $q_\omega$  value with largest spectrum area, a crucial design consideration for an efficient NFTPV system. We have found that both models predict the same structure that results in the highest  $q_\omega$  and that the

optimized structure predicted by the two models is approximately 17 nm, 49 nm, 35 nm, 11 nm, 29 nm, 14 nm, 47 nm, 27 nm, and 1043 nm, with the corresponding peak  $q_\omega$  values as shown in Fig. 4(f). In summary, both the FCN and AutoML models have demonstrated effectiveness in predicting and optimizing the structural parameters of the NFTPV system, ultimately leading to the identification of an optimized structure that maximizes the spectral radiative heat flux for enhanced energy-conversion efficiency. However, it is essential to highlight the differences in efficiency between the FCN and AutoML approaches. The FCN requires significant time investment for training the model, selecting appropriate hyperparameters, and fine tuning parameters manually. In contrast, AutoML streamlines the training process and hyperparameter tuning through NAS, offering efficient performance within a shorter time frame. This automated approach reduces the burden of manual optimization tasks associated with the FCN, making AutoML a compelling choice for rapidly achieving optimal results in NFTPV-system design and optimization.

To conclude this analysis, we have investigated the impact of radiative flux on critical parameters of the cell, namely, the short-circuit current, the electrical power, and the efficiency. We have analyzed the total flux at different vacuum gaps for two types of emitters: the SiC-plate emitter and the HMM emitter (four-period), as shown in Fig. 5(a). It can be observed that the net radiative flux decreases as the gap increases. The flux is initially higher for the HMM emitter until a 800-nm gap, beyond which

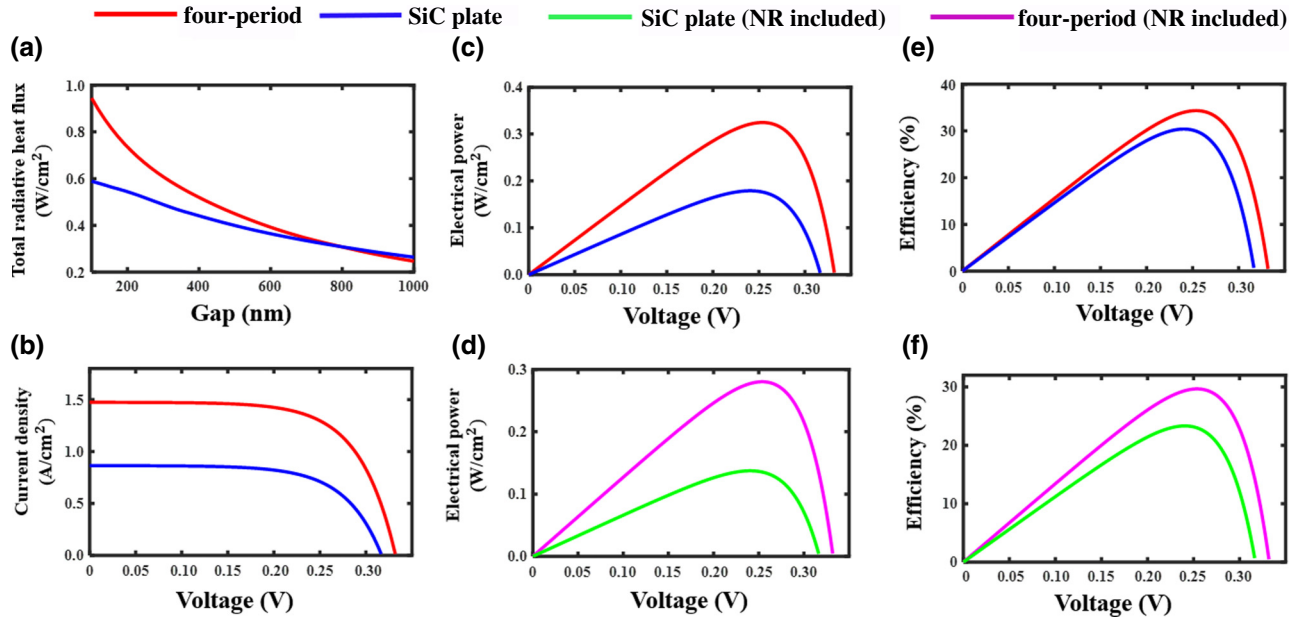


FIG. 5. A comparison of the key parameters for our designs: the HMM emitter and the SiC-plate emitter. (a) The simulated radiative heat transfer for NFTPV energy conversion at different gaps. (b) The  $J$ - $V$  characteristics obtained at a 100-nm gap. (c) The power-voltage ( $P$ - $V$ ) characteristics obtained at a 100-nm gap. (d) The electrical power considering the nonradiative effect. (e) The efficiency. (f) The efficiency considering the nonradiative effect.

TABLE I. A performance comparison of the different NFTPV-system designs.

Serial no.	$T_e$ (K)	$d$ (nm)	$P_{\text{rad}}$ (W/cm <sup>2</sup> )	$P_{\text{elec}}$ (W/cm <sup>2</sup> )	Efficiency (%)	Ref.
1	900	100	0.9452	0.324	34	Our design
2	✓	✓	✓	0.23 (NR)	30 (NR)	Our design
3	500	200	...	0.0659	...	[36]
4	✓	✓	...	0.066	...	Our design
5	1000	100	9.3	0.2	...	[34]
6	1000	100	1.33	0.4243	32	Our design
7	✓	✓	✓	0.3790	28.5 (NR)	Our design
8	2000	100	...	6.73	18	[35]
9	✓	✓	8.975	2.1	23.4	Our design

it falls below the flux obtained for the SiC-plate emitter. To maintain practicality in our design, we have maintained a minimum gap distance of 100 nm as previously stated. Next, we have examined the impact of the obtained flux on the aforementioned critical parameters of the TPV cell. We have compared the two emitter configurations (SiC plate and four-period emitter). The analysis of the photocurrent generation in the cell has been based on electrical parameters specific to the InSb cell obtained from a previous study. The methodology for this analysis follows the work described in Ref. [52]. The parameters of the InSb cell utilized in this study are taken from Refs. [53,54], with an intrinsic carrier concentration of  $n_i = 6.06 \times 10^{14} \text{ cm}^{-2}$  and Auger-recombination coefficients  $C_n = C_p = 2.26 \times 10^{-27} \text{ cm}^{-6} \text{ s}^{-1}$ .

We have first obtained the current-voltage ( $J$ - $V$ ) characteristics for the designs under consideration, as depicted in Fig. 5(b). A clear upward shift of the  $J$ - $V$  curve with a larger short-circuit current density  $J_{\text{sc}}$  can be observed for the four-period emitter compared to the SiC-plate emitter. In Fig. 5(c), we illustrate the corresponding electrical power output  $P$  at the maximum power point MPP. It is evident that  $P$  increases to  $0.324 \text{ W/cm}^2$  for the four-period emitter design compared to  $0.18 \text{ W/cm}^2$  for the SiC-plate emitter design, indicating an approximately twofold power enhancement. The efficiencies of the two designs are plotted in Fig. 5(e), with the highest recorded efficiencies being 34% and 30%, for the HMM emitter and the single-plate emitter, respectively. In addition, we have evaluated the impact of nonradiative recombination (NR) in the TPV cell on the electrical power output and efficiency, as illustrated in Figs. 5(d) and 5(f), respectively. As depicted in Fig. 5(d), when considering the NR effect, the maximum power outputs obtained are  $0.14 \text{ W/cm}^2$  for the SiC-plate emitter and  $0.28 \text{ W/cm}^2$  for the four-period emitter. Similarly, in Fig. 5(f), the maximum efficiencies recorded are 23% for the SiC-plate emitter and 30% for the four-period emitter. It can be observed that incorporating the NR effect into our calculations reflects the actual values of the electrical power output and efficiency of the TPV cell. This distinction can be attributed to variation of

the current density  $J$  with the applied voltage. Therefore, when evaluating the performance of the TPV cell, it is crucial to consider the NR. Refer to Sec. B for a more detailed analysis of the impact of  $T_e$  on the aforementioned critical parameters and Sec. C for all equations used to model the photocurrent generation in the TPV cell. Finally, we compare our results to those of some recently published papers [34–36], as shown in Table I.

### III. CONCLUSIONS

In this comparative study of the FCN and AutoML models for NFTPV-system design and optimization, we have successfully modeled the NFTPV system using the FE framework with the DGF and the SM. We have demonstrated the use of deep learning in theoretically designing and optimizing the radiative heat flux for an NFTPV system using both the FCN and AutoML models. We have also demonstrated the effect of the obtained flux on critical parameters of the TPV cell by considering the inclusion of NR and its exclusion. To effectively communicate the challenges and limitations that we have encountered while using deep-learning models for optimizing the spectral radiative heat flux in an NFTPV system, it is crucial to highlight the following. The generation of training sets is a time-consuming process, which may become even more demanding as the period of the hyperbolic emitter increases. The architecture models that we have employed could accurately represent the ground-truth spectrum for any structure within the design space. However, they could not accurately represent the ground-truth spectrum for structures outside the design space. It is crucial to ensure that the models can accurately represent spectra for structures both within and outside the design space.

### IV. METHODS

#### A. Modeling of dielectric function and formation of hyperbolic bands

Doped silicon (DSi) is used as the metallic layer, the dielectric model can be found in Ref. [55], while



silicon carbide (SiC) is used as the dielectric layer and is described by Eq. (1) with  $\varepsilon_\infty = 6.7$ ,  $\omega_L = 1.8 \times 10^{14} \text{ s}^{-1}$ ,  $\omega_T = 1.49 \times 10^{14} \text{ s}^{-1}$ , and  $\gamma = 8.9 \times 10^{11} \text{ s}^{-1}$  [56]:

$$\varepsilon_{\text{SiC}} = \varepsilon_\infty + \frac{\varepsilon_\infty(\omega_L^2 - \omega_T^2)}{\omega_T^2 - \omega^2 - i\gamma\omega}. \quad (1)$$

The periodic layers (DSi and SiC) are deposited on a semi-infinite SiC layer that serves as a substrate. The receiver (TPV cell) consists of an indium antimonide (InSb) on a semi-infinite aluminum (Al) layer, serving as an electrode. The InSb layer is modeled as [53]

$$\varepsilon_{\text{cell}} = \left( n + \frac{i\alpha}{2k_0} \right)^2, \quad (2)$$

where  $\alpha$  is given as

$$\alpha(\omega) = \begin{cases} 0, & \omega < E_g, \\ \alpha_0 \sqrt{\frac{\omega - E_g}{E_g}}, & \omega \geq E_g. \end{cases} \quad (3)$$

### B. Theoretical modeling of a NFTPV system

The general expression for the spectral radiative heat flux between planar surfaces based on Rytov's FE and the DGF is given as [57–61]:

$$q_\omega(T_e, T_r, d) = \frac{1}{4\pi^2} (\Theta(\omega, T_e) - \Theta(\omega, T_r)) \times \int_0^\infty d\beta \beta (\xi_{\text{TE}}(\omega, \beta) + \xi_{\text{TM}}(\omega, \beta)), \quad (4)$$

where  $\Theta(\omega, T)$  is the Planck mean oscillator energy, given as

$$\Theta(\omega, T) = \frac{\hbar\omega}{e^{\frac{\hbar\omega}{k_B T}} - 1}, \quad (5)$$

$\xi_\alpha$  is the photonic transmission coefficient, expressed as

$$\xi_\alpha(\omega, k) = \begin{cases} \frac{(1 - |R_\alpha^e|^2)(1 - |R_\alpha^r|^2)}{|D_\alpha|^2}, & \beta < k_0, \\ \frac{4 \text{Im}(R_\alpha^e) \text{Im}(R_\alpha^r) e^{-2 \text{Im}(k_z^0) d}}{|D_\alpha|^2}, & \beta > k_0, \end{cases} \quad (6)$$

which considers contributions of both propagating ( $\beta < k_0$ ) and evanescent ( $\beta > k_0$ ) waves, and  $\alpha$  represents TE or TM modes. The contribution of the evanescent field results in super-Planckian heat transfer at the nanoscale gap [58].  $T_e$  is the emitter temperature (at 900 K),  $T_r$  is the receiver temperature (maintained at 300 K), and

$k_{z0} = \sqrt{(k_0^2 - \beta^2)}$ ,  $k_0 = \omega/c$ ,  $D_\alpha = 1 - R_\alpha^e R_\alpha^r e^{-2ik_{z0}d}$ , and  $\beta$  are perpendicular wave vectors in a vacuum, the vacuum wave vector, the Fabry-Perot-like denominator, and the wave vector parallel to the multilayer stacks, respectively.  $R_\alpha^e$  and  $R_\alpha^r$  denote the reflection coefficient amplitude for the multilayer structure emitter and the receiver as viewed from the vacuum. We adopt the procedure described by Raphael *et al.* for calculating  $R_\alpha$  in our analysis, as the method has been proven stable when dealing with high a  $\beta$  value for the evanescent field and highly absorbing materials [50]. Finally, the total radiative flux  $Q$  can be obtained from

$$Q(T, d) = \int_0^\infty d\omega q_\omega(T_e, T_r, d). \quad (7)$$

### ACKNOWLEDGMENTS

This work was supported by the Australian Research Council Discovery Project (Grant No. DP200101353).

### APPENDIX A: TOTAL REFLECTION COEFFICIENT FOR A MULTILAYER STRUCTURE

The reflection coefficients of a multilayer hyperbolic emitter and the receiver (the TPV cell) can be determined using an optical-multilayer algorithm [50]. This algorithm takes into account the refractive indices of the layers and a parallel wave vector ( $\beta$ ). The multilayer stack consists of  $N$  interfaces, numbered from 1 to  $N$ , with the incidence interface denoted as 0 and the output medium denoted as  $N$ . In this particular case, the output medium of the emitter and the receiver is represented by SiC and Al, respectively, as shown in Fig. 1(a). The reflection coefficient for the emitter or TPV cell, as viewed from vacuum (the incident medium), can be calculated recursively using Eq. (A1), starting at the last interface (the  $N$  th) and working backward to the incidence interface. The initial condition is set to  $R_N = r_N$ :

$$R_j = \frac{r_j + R_{j+1} e^{2i\sqrt{k_j^2 - \beta^2} t_j}}{1 + r_j R_{j+1} e^{2i\sqrt{k_j^2 - \beta^2} t_j}}, \quad (A1)$$

$$r_j^{\text{TE}} = \frac{\sqrt{k_j^2 - \beta^2} - \sqrt{k_{j+1}^2 - \beta^2}}{\sqrt{k_j^2 - \beta^2} + \sqrt{k_{j+1}^2 - \beta^2}}, \quad (A2)$$

$$r_j^{\text{TM}} = \frac{\frac{k_{j+1}}{k_j} \sqrt{k_j^2 - \beta^2} - \frac{k_j}{k_{j+1}} \sqrt{k_{j+1}^2 - \beta^2}}{\frac{k_{j+1}}{k_j} \sqrt{k_j^2 - \beta^2} + \frac{k_j}{k_{j+1}} \sqrt{k_{j+1}^2 - \beta^2}}. \quad (A3)$$

Equation (A1) calculates the total reflection coefficient for a given interface, where  $t_j$  is the thickness of the  $j$  th layer in nanometers,  $r_j$  is the Fresnel reflection coefficient of

the  $j$ th interface, and  $k_j$  is the wave vector in the  $j$ th medium. The values of  $r_j$  for TE and TM modes are given by Eqs. (A2) and (A3), respectively.

## APPENDIX B: THEORETICAL MODELING OF NFTPV SYSTEM

In this appendix, we have examined the influence of an increased doping concentration  $N_c$  of DSi on the net heat flux  $Q$  for one-period, two-period, and four-period HMM emitters across various gap distances at  $T_e$  of 900 K. To provide a comprehensive comparison, we have contrasted the obtained results with those from single-plate emitters, illustrated in Fig. 6(a). Notably, it is evident that the HMM emitters exhibit higher  $Q$  values compared to a single-plate emitter. Conversely, the SiC-plate emitter consistently records the lowest  $Q$  values across the gap variations. As detailed in the main text, at a 100-nm gap, the four-period HMM emitter consistently displays the highest  $Q$  values when compared to other emitter configurations. Furthermore, we have investigated the effect of varying  $T_e$  on  $Q$ , as depicted in Fig. 6(b), when  $d$  is kept at 100 nm. As anticipated, an increase in emitter temperature correlates with an augmentation of  $Q$ , with the four-period emitter consistently attaining peak values across the entire temperature range. Lastly, we examine the effect of varying doping concentrations on  $Q$  for different periods of hyperbolic emitters, as illustrated in Fig. 6(c). The results show that  $Q$  increases with an increase in  $N_c$ , with the four-period configuration yielding the highest values. These findings highlight the advantage of utilizing a hyperbolic emitter in achieving comparable heat flux at greater gap

distances compared to single-plate emitters. Recognizing the importance of the ability of the model to distinguish between different input layers, we have performed an analysis on the response of the model to varying structural layers and the results are shown in Figs. 7(a)–(e). Additionally, we have obtained the corresponding net flux and we represent the results as a bar graph in Fig. 7(f).

## APPENDIX C: MODELING OF PHOTOCURRENT GENERATION IN TPV CELL

We have modeled the photocurrent generation inside the TPV cell with and without the inclusion of nonradiative recombination (NR). The NR current density is given by Ref. [62]:

$$J_{\text{nr}} = q t_r (C_n + C_p) n_i^3 \exp\left(\frac{3qV}{2k_B T_r}\right). \quad (\text{C1})$$

The total current density with inclusion of NR ( $J_{\text{NR}}$ ) and without NR ( $J_{\text{NR}}^*$ ) are expressed, respectively, as follows:

$$J_{\text{NR}} = J_{\text{ph}} - J_{\text{rad}} - J_{\text{nr}}, \quad (\text{C2})$$

$$J_{\text{NR}}^* = J_{\text{ph}} - J_{\text{rad}}, \quad (\text{C3})$$

where  $n_i$  is the intrinsic carrier concentration,  $k_B$  is the Boltzmann constant,  $q$  is the electronic charge,  $t_r$  is the thickness of the cell,  $C_n$  and  $C_p$  are Auger-recombination coefficients,  $V$  is the applied voltage,  $T_r$  is the cell temperature,  $J_{\text{ph}}$  is the photon current density, and  $J_{\text{rad}}$  is the radiative current density.  $J_{\text{ph}}$  and  $J_{\text{rad}}$  can be calculated,

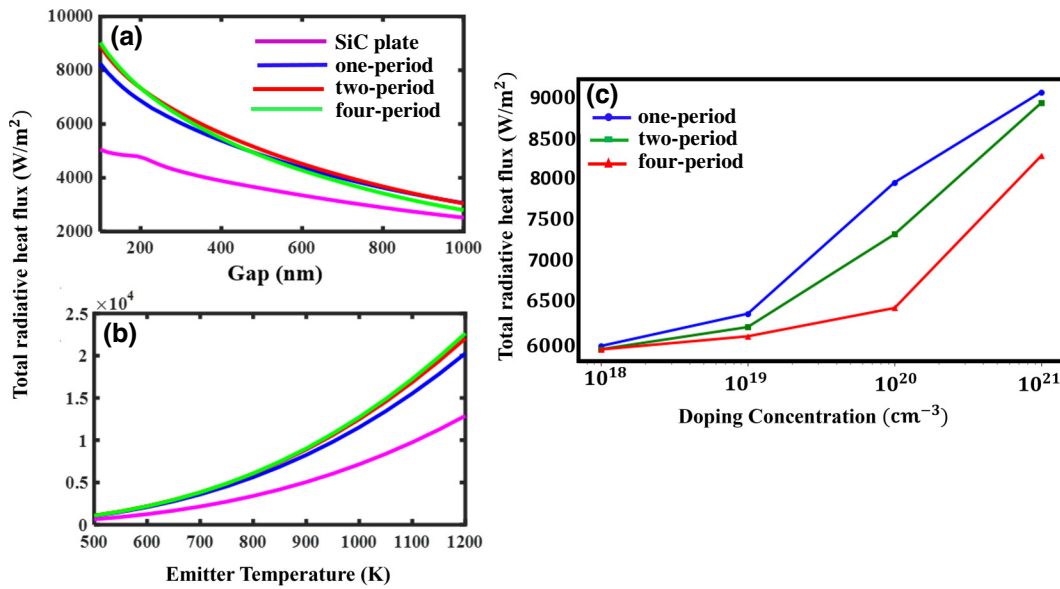


FIG. 6. (a) The net radiative heat flux at different gaps for the different emitter designs at  $N_c = 10^{21}$  when  $T_e = 900$  K. (b) The net radiative heat flux at different emitter temperatures for different designs at  $N_c = 10^{21}$  at a 100-nm gap. (c) The net radiative heat flux at different doping concentrations for different hyperbolic emitters when  $T_e = 900$  K at the 100-nm gap.

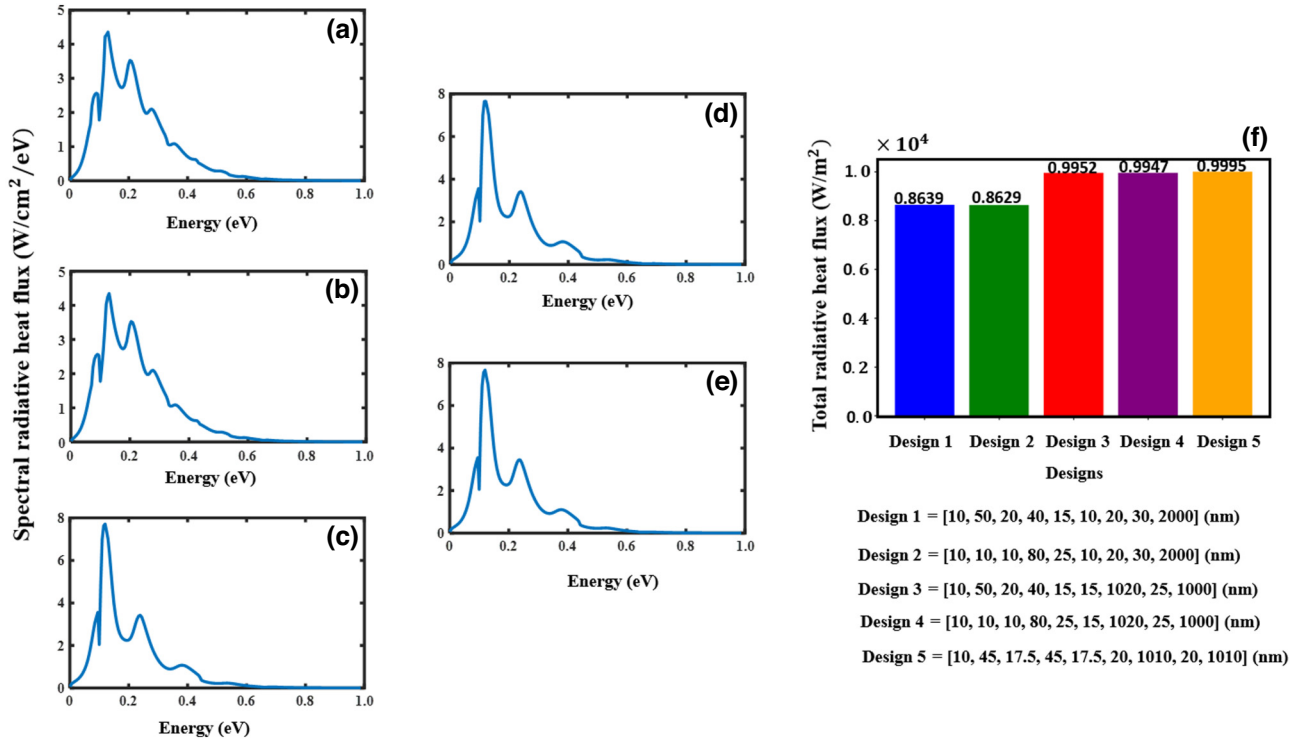


FIG. 7. The effect of varying layer thickness on the spectral heat flux (a) design 1, (b) design 2, (c) design 3, (d) design 4, (e) design 5. (f) A bar graph showing the net flux for different structures.

respectively, as follows:

$$J_{\text{ph}} = \int_{\omega_c}^{\infty} \frac{q}{4\pi^2 \omega \hbar} (\Theta(\omega, T_e, 0)) \times \int_0^{\infty} d\beta \beta (\xi_{\text{TE}}(\omega, \beta) + \xi_{\text{TM}}(\omega, \beta)) d\omega, \quad (\text{C4})$$

$$J_{\text{rad}} = \int_{\omega_c}^{\infty} \frac{q}{4\pi^2 \omega \hbar} (\Theta(\omega, T_r, V)) \times \int_0^{\infty} d\beta \beta (\xi_{\text{TE}}(\omega, \beta) + \xi_{\text{TM}}(\omega, \beta)) d\omega, \quad (\text{C5})$$

where  $\omega_c$  is the angular frequency in rad/s corresponding to the band gap of the InSb cell ( $E_{\text{gap}} = 0.17$  eV) at room temperature. Finally, the efficiency of the overall system can be calculated as follows:

$$\text{efficiency} = \frac{P}{Q} \times 100, \quad (\text{C6})$$

where  $P$  is the output power density of the cell and  $Q$  is the total radiative heat flux obtained by integrating  $q_{\omega}(T_e, T_r, d)$  over the entire frequency range:

$$P = \begin{cases} J_{\text{NR}} V, & \text{with NR,} \\ J_{\text{NR}^*} V, & \text{otherwise.} \end{cases} \quad (\text{C7})$$

We have conducted an analysis of the electrical power and efficiency of two different emitter designs: the HMM emitter with a four-period structure and the single-plate emitter with the SiC plate. We have considered two cases for each emitter design, one with the inclusion of NR and one by excluding it.

The plots in Figs. 8(a) and 8(b) illustrate the relationship between the electrical power and the applied voltage for both emitter designs. The maximum power densities achieved are 0.324 W/cm² (excluding NR) and 0.28 W/cm² (including NR) for the four-period emitter, while for the SiC-plate emitter, the values are 0.18 W/cm² (excluding NR) and 0.14 W/cm² (including NR). Furthermore, we have assessed the efficiency of the emitter designs. For the four-period emitter, the efficiencies are 34% (excluding NR) and 30% (including NR), while for the SiC-plate emitter, the efficiencies are 30% (excluding NR) and 23% (including NR), as depicted in Figs. 8(c) and 8(d). This highlights the importance of considering the effect of NR when evaluating the figure of merit (FoM) for a TPV system.

In order to understand the influence of the gap variation on the electrical power output and current density of the optimized four-period emitter in a TPV system, we have conducted a study in which we have obtained  $J$ - $V$  curves at different vacuum gaps. As expected, as the gap decreases,  $P$  experiences a substantial increase. At gap

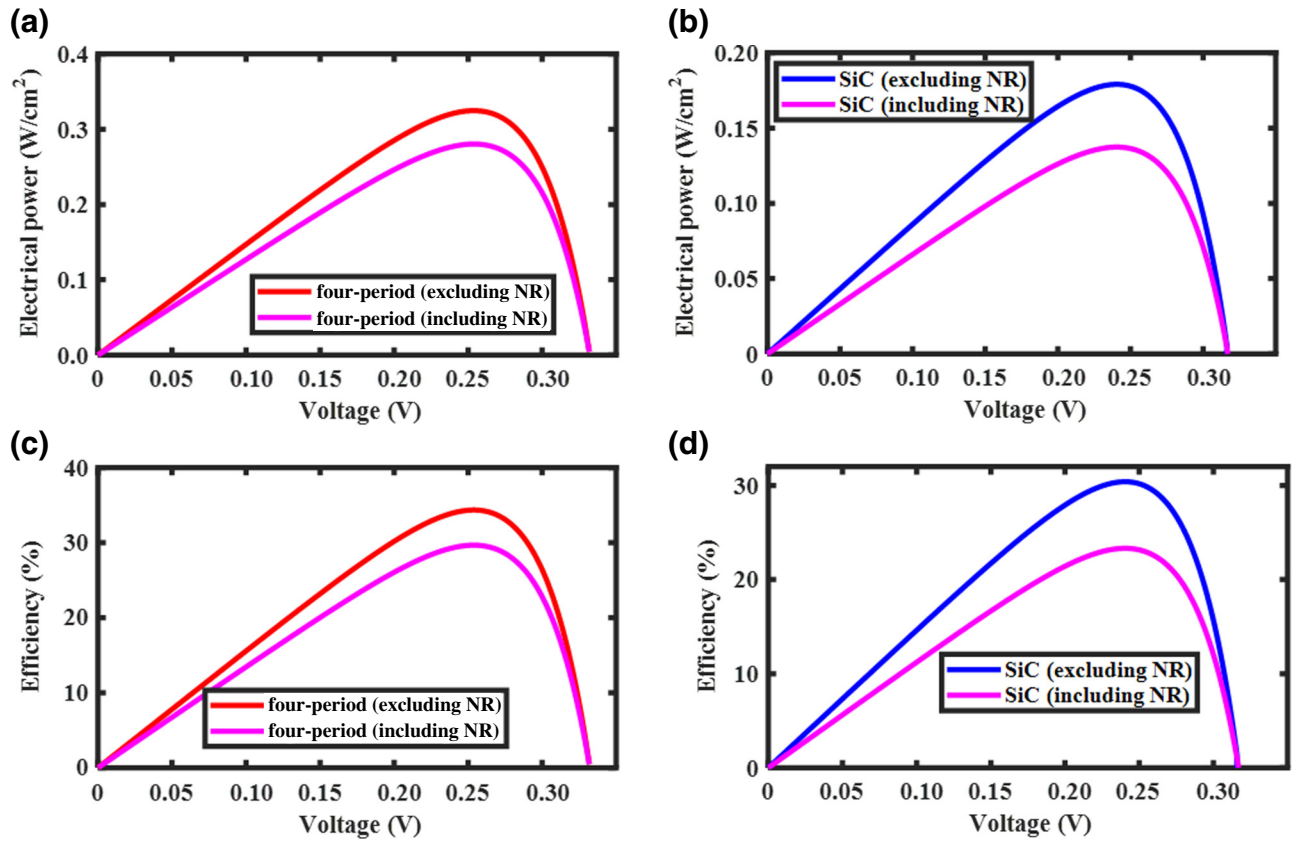


FIG. 8. Evaluation of the key parameters of the cell with and without NR. (a) The power density for the four-period emitter. (b) The power density for the SiC-plate emitter. (c) The efficiency for the four-period emitter. (d) The efficiency for the SiC-plate emitter.

sizes of 100 nm and 500 nm,  $P$  measures 0.324 W/cm<sup>2</sup> and 0.15 W/cm<sup>2</sup>, respectively. We have also obtained the corresponding current-density characteristics for gaps of 100

nm and 500 nm. Notably, as the gap size decreases, there is a noticeable upward shift of the  $J$ - $V$  curve toward a larger short-circuit current density  $J_{sc}$ . For instance,  $J_{sc}$  increases

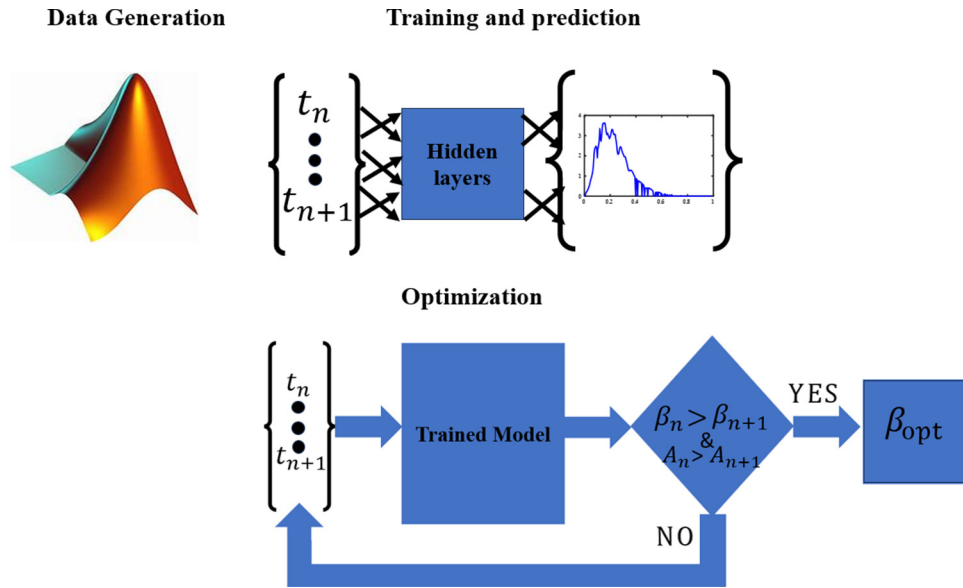


FIG. 9. A schematic diagram for implementation of the deep-learning approach.



from 0.74 A/cm<sup>2</sup> at 500 nm to 1.5 A/cm<sup>2</sup> at 100 nm. This increase can be attributed to the higher above-band-gap (ABG) photon flux resulting from the coupling of evanescent modes at subwavelength gaps. This demonstrates the enhancement of both  $P$  and  $J$  with increasing gap size.

Finally, in Fig. 9 we illustrate the deep-learning approach employed in this study. The schematic diagram is structured into three key stages: data generation, training and predictions, and optimization. Data generation involves utilizing the MATLAB simulation software to generate data by varying the structural parameters of the NFTPV system under investigation. The training process differs for the two ML models used: manual training for the FCN and automated training for AutoML. During this stage, the models are trained to predict the spectrum, specifically the spectral radiative heat flux, by minimizing the mean absolute error (MAE). Following successful training, the models are used for spectrum prediction. Lastly, an optimization process is implemented using an iterative algorithm, as depicted in Fig. 9. This optimization aims to compare different generated spectra and identify the spectrum with the maximum flux and area as the output. This is crucial for achieving a high net flux, which translates to a higher number of ABG photons, ultimately contributing to a more efficient NFTPV system.

- [1] A. Fiorino, L. Zhu, D. Thompson, R. Mittapally, P. Reddy, and E. Meyhofer, Nanogap near-field thermophotovoltaics, *Nat. Nanotechnol.* **13**, 806 (2018).
- [2] G. R. Bhatt, B. Zhao, S. Roberts, I. Datta, A. Mohanty, T. Lin, J. M. Hartmann, R. St-Gelais, S. Fan, and M. Lipson, Integrated near-field thermo-photovoltaics for heat recycling, *Nat. Commun.* **11**, 2545 (2020).
- [3] T. Inoue, T. Koyama, D. D. Kang, K. Ikeda, T. Asano, and S. Noda, One-chip near-field thermophotovoltaic device integrating a thin-film thermal emitter and photovoltaic cell, *Nano Lett.* **19**, 3948 (2019).
- [4] C. Lucchesi, D. Cakiroglu, J. P. Perez, T. Taliercio, E. Tournie, P. O. Chapuis, and R. Vaillon, Near-field thermophotovoltaic conversion with high electrical power density and cell efficiency above 14%, *Nano Lett.* **21**, 4524 (2021).
- [5] R. Mittapally, B. Lee, L. Zhu, A. Reihani, J. W. Lim, D. Fan, S. R. Forrest, P. Reddy, and E. Meyhofer, Near-field thermophotovoltaics for efficient heat to electricity conversion at high power density, *Nano Commun.* **12**, 4364 (2021).
- [6] J. B. Pendry, Radiative exchange of heat between nanostructures, *J. Phys.: Condens. Matter* **11**, 6621 (1999).
- [7] K. Achim, M.-H. Wolfgang, P. Jürgen, B. Svend-Age, R. Daniel, and H. Martin, Near-field heat transfer in a scanning thermal microscope, *Phys. Rev. Lett.* **95**, 224301 (2005).
- [8] D. Wilde, Y. Formanek, F. Carminati, R. Gralak, L. B. P. A. Joulain, M. K. J. P. Chen, Y. Greffet, and M. J. J., Thermal radiation scanning tunnelling microscopy, *Nature* **444**, 7120 (2006).
- [9] A. Kittel, U. F. Wischnath, J. Welker, O. Huth, F. Rütting, and S.-A. Biehs, Near-field thermal imaging of nanostructured surfaces, *Appl. Phys. Lett.* **93**, 193109 (2008).
- [10] M. H. Kryder, E. C. Gage, T. W. McDaniel, W. A. Challenor, R. E. Rottmayer, G. Ju, Y.-T. Hsia, and M. F. Erden, Heat assisted magnetic recording, *Proc. IEEE* **96**, 1810 (2008).
- [11] M. Grajower, B. Desiatov, I. Goykhman, L. Stern, N. Mazurski, and U. Levy, Direct observation of optical near field in nanophotonics devices at the nanoscale using scanning thermal microscopy, *Opt. Express* **23**, 27763 (2015).
- [12] P. J. Van Zwol, K. Joulain, P. Ben-Abdallah, and J. Chevrier, Phonon polaritons enhance near-field thermal transfer across the phase transition of VO<sub>2</sub>, *Phys. Rev. B* **84**, 161413 (2011).
- [13] Y. Tian, A. Ghanekar, L. Qian, M. Ricci, X. Liu, G. Xiao, O. J. Gregory, and Y. Zheng, Near-infrared optics of nanoparticles embedded silica thin films., *Opt. Express* **27**, A148 (2019).
- [14] S. Vassant, I. Doyen, F. Marquier, F. Pardo, U. Gennser, A. Cavanna, J. Luc Pelouard, and J.-J. Greffet, Electrical modulation of emissivity, *Appl. Phys. Lett.* **102**, 081125 (2013).
- [15] A. A. Odebowale, A. M. Berhe, H. T. Hattori, and A. E. Miroshnichenko, Modeling and analysis of a radiative thermal memristor, *Appl. Sci.* **14**, 2633 (2024).
- [16] V. B. Svetovoy and G. Palasantzas, Graphene-on-silicon near-field thermophotovoltaic cell, *Phys. Rev. Appl.* **2**, 034006 (2014).
- [17] J. H. Lee, I. Bargatin, N. A. Melosh, and R. T. Howe, Optimal emitter-collector gap for thermionic energy converters, *Appl. Phys. Lett.* **100**, 173904 (2012).
- [18] K. Park, S. Basu, W. King, and Z. Zhang, Performance analysis of near-field thermophotovoltaic devices considering absorption distribution, *J. Quant. Spectrosc. Radiat. Transf.* **109**, 305 (2008).
- [19] M. Laroche, R. Carminati, and J.-J. Greffet, Coherent thermal antenna using a photonic crystal slab, *Int. J. Energy Res.* **96**, 123903 (2006).
- [20] S. Basu, Z. M. Zhang, and C. J. Fu, Review of near-field thermal radiation and its application to energy conversion, *Int. J. Energy Res.* **33**, 1203 (2009).
- [21] M. Lim, J. Song, S. Lee, and B. Lee, Tailoring near-field thermal radiation between metallo-dielectric multilayers using coupled surface plasmon polaritons, *Nat. Commun.* **9**, 2041 (2018).
- [22] J. Yang, W. Du, Y. Su, Y. Fu, S. Gong, S. He, and Y. Ma, Observing of the super-Planckian near-field thermal radiation between graphene sheets, *Nat. Commun.* **9**, 4033 (2018).
- [23] J. C. Cuevas and F. J. Garcia-Vidal, Radiative heat transfer, *ACS Photonics* **5**, 3896 (2018).
- [24] S. A. Biehs, R. Messina, P. S. Venkataram, A. W. Rodriguez, J. C. Cuevas, and P. Ben-Abdallah, Near-field radiative heat transfer in many-body systems, *Rev. Mod. Phys.* **93**, 025009 (2021).
- [25] R. Mittapally, A. Majumder, P. Reddy, and E. Meyhofer, Near-field thermophotovoltaic energy conversion: Progress and opportunities, *Phys. Rev. Appl.* **19**, 037002 (2023).

- [26] L. Zhang and O. D. Miller, Optimal materials for maximum large-area near-field radiative heat transfer, *ACS Photonics* **7**, 3116 (2020).
- [27] M. Francoeur, M. P. Menguc, and R. Vaillon, Near-field radiative heat transfer enhancement via surface phonon polaritons coupling in thin films, *Appl. Phys. Lett.* **93**, 043109 (2008).
- [28] P. Ben-Abdallah, K. Joulain, J. Drevillon, and G. Domingues, Near-field heat transfer mediated by surface wave hybridization between two films, *J. Appl. Phys.* **106**, 044306 (2009).
- [29] H. Iizuka and S. Fan, Significant enhancement of nearfield electromagnetic heat transfer in a multilayer structure through multiple surface-states coupling, *Phys. Rev. Lett.* **120**, 063901 (2018).
- [30] V. Fernandez-Hurtado, F. J. Garcia-Vidal, S. H. Fan, and J. C. Cuevas, Enhancing near-field radiative heat transfer with Si-based metasurfaces, *Phys. Rev. Lett.* **118**, 203901 (2017).
- [31] L. Liu, R. Z. Zhang, and Z. M. Zhang, Nearfield radiative heat transfer with doped-silicon nanostructured metamaterials, *Int. J. Heat Mass Transfer* **73**, 389 (2014).
- [32] S. A. Biehs, R. Messina, P. S. Venkataram, A. W. Rodriguez, J. C. Cuevas, and P. Ben-Abdallah, Near-field radiative heat transfer in many-body systems, *Rev. Mod. Phys.* **93**, 025009 (2021).
- [33] H. Iizuka and S. Fan, Significant enhancement of near-field electromagnetic heat transfer in a multilayer structure through multiple surface-states coupling, *Phys. Rev. Lett.* **120**, 063901 (2018).
- [34] S. Jin, M. Lim, S. S. Lee, and B. J. Lee, Hyperbolic metamaterial-based near-field thermophotovoltaic system for hundreds of nanometer vacuum gap, *Opt. Express* **24**, A635 (2016).
- [35] A. Datas and R. Vaillon, Thermionic-enhanced nearfield thermophotovoltaics for medium-grade heat sources, *Appl. Phys. Lett.* **114**, 133501 (2019).
- [36] M. Lim, J. Song, J. Kim, S. S. Lee, I. Lee, and B. J. Lee, Optimization of a near-field thermophotovoltaic system operating at low temperature and large vacuum gap, *J. Quant. Spectrosc. Radiat. Transf.* **210**, 35 (2018).
- [37] G. Hinton, L. Deng, D. Yu, G. E. Dahl, A. Mohamed, N. Jaitly, A. Senior, V. Vanhoucke, P. Nguyen, T. N. Sainath, and B. Kingsbury, Deep neural networks for acoustic modeling in speech recognition: The shared views of four research groups, *IEEE Signal Proc. Mag.* **29**, 82 (2012).
- [38] P. Mehta, M. Bukov, C.-H. Wang, A. G. Day, C. Richardson, C. K. Fisher, and D. J. Schwab, A high-bias, low-variance introduction to machine learning for physicists, *Phys. Rep.* **810**, 1 (2019).
- [39] G. Carleo, I. Cirac, K. Cranmer, L. Daudet, M. Schuld, N. Tishby, L. Vogt-Maranto, and L. Zdeborová, Machine learning and the physical sciences, *Rev. Mod. Phys.* **91**, 045002 (2019).
- [40] R. Li, Z. Liu, A. Rohskopf, K. Gordiz, A. Henry, E. Lee, and T. Luo, A deep neural network interatomic potential for studying thermal conductivity of  $\beta$ -Ga<sub>2</sub>O<sub>3</sub>, *Appl. Phys. Lett.* **15**, 152102 (2020).
- [41] J. García-Esteban, J. Bravo-Abad, and J. Cuevas, Deep learning for the modeling and inverse design of radiative heat transfer, *Phys. Rev. Appl.* **16**, 064006 (2021).
- [42] Z. Liu, Z. Zhang, P. Xie, and Z. Miao, Design of selective TPV thermal emitters based on Bayesian optimization nesting simulated annealing, *Energies* **16**, 416 (2023).
- [43] A. A. Odebowale, S. Abdo, N. Alim, K. As'ham, H. T. Hattori, and A. E. Miroshnichenko, in *2023 IEEE Photonics Conference (IPC)* (IEEE, Orlando, FL, 2023), pp. 1–2.
- [44] S. Wen, C. Dang, and X. Liu, A machine learning strategy for modeling and optimal design of near-field radiative heat transfer, *Appl. Phys. Lett.* **121**, 071101 (2022).
- [45] A. Vlasov, Obtaining silicon carbide from rice husks, *Refract. Ind. Ceram.* **32**, 9 (1991).
- [46] Y. Zhong, L. L. Shaw, M. Manjarres, and M. F. Zawrah, Synthesis of silicon carbide nanopowder using silica fume, *J. Am. Ceram. Soc.* **93**, 3159 (2010).
- [47] S. Basu, B. J. Lee, and Z. M. Zhang, Infrared radiative properties of heavily doped silicon at room temperature, *J. Heat Transf.—Trans. ASME* **132**, 023301 (2010).
- [48] S.-A. Biehs and P. Ben-Abdallah, Near-field heat transfer between multilayer hyperbolic metamaterials, *Z. Naturforsch. A* **72**, 115 (2017).
- [49] S. Lang, H. Lee, A. Petrov, M. Störmer, M. Ritter, and M. Eich, Gold-silicon metamaterial with hyperbolic transition in near infrared, *Appl. Phys. Lett.* **103**, 021905 (2013).
- [50] R. St-Gelais, G. R. Bhatt, L. Zhu, S. Fan, and M. Lipson, Hot carrier-based near-field thermophotovoltaic energy conversion, *ACS Nano* **11**, 3001 (2017).
- [51] M. Lim, J. Song, S. S. Lee, and B. J. Lee, Tailoring near-field thermal radiation between metallo-dielectric multilayers using coupled surface plasmon polaritons, *Nat. Commun.* **9**, 4302 (2018).
- [52] D. Feng, E. J. Tervo, S. K. Yee, and Z. M. Zhang, Effect of evanescent waves on the dark current of thermophotovoltaic cells, *Nanoscale Microscale Thermophys. Eng.* **24**, 1 (2020).
- [53] O. Ilic, M. Jablan, J. D. Joannopoulos, I. Celanovic, and M. Soljačić, Overcoming the black body limit in plasmonic and graphene near-field thermophotovoltaic systems, *Opt. Express* **20**, A366 (2012).
- [54] Y. Sheng, Enhancement of a graphene-based near-field thermophotovoltaic system by optimization algorithms and dynamic regulations, *Photonics* **10**, 137 (2023).
- [55] S. Basu, B. J. Lee, and Z. M. Zhang, Near-field radiation calculated with an improved dielectric function model for doped silicon, *J. Heat Transf.* **132**, 023301 (2010).
- [56] A. I. Volokitin and B. N. J. Persson, Near-field radiative heat transfer and noncontact friction, *Rev. Mod. Phys.* **79**, 1291 (2007).
- [57] S.-A. Biehs, P. Ben-Abdallah, F. S. S. Rosa, K. Joulain, and J.-J. Greffet, Nanoscale heat flux between nanoporous materials, *Opt. Express* **19**, A1088 (2011).
- [58] D. Polder and M. Van Hove, Theory of radiative heat transfer between closely spaced bodies, *Phys. Rev. B* **4**, 3303 (1971).
- [59] A. A. Orlov, P. M. Voroshilov, P. A. Belov, and Y. S. Kivshar, Engineered optical nonlocality in nanostructured metamaterials, *Phys. Rev. B* **84**, 045424 (2011).

- [60] M. Krüger, G. Bimonte, T. Emig, and M. Kardar, Trace formulas for nonequilibrium Casimir interactions, heat radiation, and heat transfer for arbitrary objects, [Phys. Rev. B \*\*86\*\*, 115423 \(2012\)](#).
- [61] G. Bimonte and E. Santamato, General theory of electromagnetic fluctuations near a homogeneous surface in terms of its reflection amplitudes, [Phys. Rev. A \*\*76\*\*, 013810 \(2007\)](#).
- [62] B. Roy-Layinde, T. Burger, D. Fan, B. Lee, S. McSherry, S. R. Forrest, and A. Lenert, Sustaining efficiency at elevated power densities in InGaAs airbridge thermophotovoltaic cells, [Sol. Energy Mater. Sol. Cells \*\*236\*\*, 111523 \(2022\)](#).